Visualizing Intrinsic 3D-Strain Distribution in Gold Coated ZnO Microstructures by Bragg Coherent X-Ray Diffraction Imaging and Transmission Electron Microscopy with Respect to Piezotronic Applications

Philipp Jordt, Niklas Wolff, Stjepan B. Hrkac, Sindu Shree, Di Wang, Ross J. Harder, Christian Kübel, Rainer Adelung, Oleg G. Shpyrko, Olaf M. Magnussen, Lorenz Kienle, and Bridget M. Murphy*

Novel devices ranging from bio magnetic field sensors to energy harvesting nano machines utilize the piezotronic effect. For optimal function, understanding the interaction of electrical and strain phenomena within the semiconductor crystal is necessary. Here, studies of a model piezotronic system are presented, consisting of a ZnO microrod coated by a thin layer of gold, which forms a Schottky contact with the piezoelectric ZnO material. Coherent X-ray diffraction imaging (CXDI) and transmission electron microscopy (TEM) are used to visualize the structure and strain distribution, showing that the ZnO microrod exhibits strains of multiple origins in the bulk and at the interface. Strain values of -6×10^{-4} have been measured by CXDI at the ZnO/Au interface. The origin is shown to be a combination of an interface strain, possibly caused by the Schottky contact formation, and distinct, localized electrical fields inside the crystal which are assigned to electron depletion and screening in a bent ZnO/Au piezotronic rod. These findings will contribute to sensor development and to a better understanding of piezotronic applications.

1. Introduction

In the future, emerging technologies with semiconductor-based smart devices may include artificial skin,[1] synapsis,[2] energy harvesting,[3,4] and magnetoelectric applications that rely on composites of piezoelectric and magnetostrictive materials.[5–7] A specific example for potential medical application is a small, highly sensitive magnetoelectric sensor capable to measure the low frequency magnetic fields originating in the human body.[8] As these fields are really small in the pT to fT range, a promising approach to increase the sensitivity might be to exploit the piezotronic effect as a source of intrinsic signal amplification.[9–12] The piezotronic effect is found in piezoelectric semiconductors and combines the piezoelectric effect with the electric behavior of a Schottky contact at a

P. Jordt, O. M. Magnussen, B. M. Murphy
Institute of Experimental and Applied Physics
Kiel University
Leibnizstr. 19, 24118 Kiel, Germany
E-mail: murphy@physik.uni-kiel.de

O. M. Magnussen, B. M. Murphy
Ruprecht-Haensel Laboratory
Kiel University
24118 Kiel, Germany

N. Wolff, R. Adelung, L. Kienle
Institute of Material Sciences
Kiel University
Kaiserstr. 2, 24143 Kiel, Germany

S. B. Hrkac, O. G. Shpyrko
Department of Physics
University of California San Diego
La Jolla, CA 92093, USA

S. Shree
Institute of Inorganic Chemistry and Crystallography
University of Bremen
Leobenerstr. NW2, 28359 Bremen, Germany

R. J. Harder
X-ray Sciences Division
Argonne National Laboratory
Lemont, IL 60439, USA

D. Wang, C. Kübel
Institute of Nanotechnology & Karlsruhe Nano Micro Facility (KNMF)
Karlsruhe Institute of Technology (KIT)
Hermann-von-Helmholtz-Platz 1, 76344 Eggenstein-Leopoldshafen, Germany

C. Kübel
Department of Materials & Earth Sciences
Technical University Darmstadt
64287 Darmstadt, Germany

**ADVANCED
SCIENCE NEWS**
www.advancedsciencenews.com

**ADVANCED
ELECTRONIC
MATERIALS**
www.advelectronicmat.de

semiconductor/metal interface.[13–15] External stress and crystal quality induce a strong electric response in piezoelectric semiconductors, changing the height of the Schottky barrier and the depletion width.[16,17] By the addition of a magnetostrictive material, the variation of external magnetoelastic stress imposed on the semiconductor material could further tune the conductivity across the Schottky barrier for potential sensor applications.

The majority of studies on the piezotronic effect concentrate on electrical characterization and employ predominantly ZnO, which is a well-known piezoelectric material with wurtzite-type crystal structure. These studies emphasized the direct influence of external mechanical stress on the Schottky barrier height in ZnO bulk[16] and microstructures[18,19] when stress is applied along the ZnO c–axis. Choosing the direction of applied stress can induce either tensile or compressive stresses which increase or decrease the Schottky barrier height accordingly.[20]

Additionally, it was shown that strain and an associated E-field can be induced by bending free-standing ZnO micro rods using an atomic force microscope.[21] The resulting change in conductivity was assigned to formation of a depletion region, thus shrinking the conduction channel size inside the rod. Combined analytical calculations and finite element method simulations, confirm that bending of ZnO wires leads to a negative potential at the compressed side and a positive potential on the relaxed side of the rod.[22] Further calculations considering n-type ZnO, indicate that the positive potential inside the ZnO rod is partly or fully screened, depending on the donor electron concentration.[23]

Previous studies by the authors already showed a complex strain behavior in ZnO micro rods.[24,25] FeCoSiB coated ZnO rods were investigated in detail by scanning nano X-ray diffraction (XRD). The strain was found to be non-uniform, with an asymmetric strain variation at the rod edges and a strong dependence of the strain profile on the aspect ratio. Two strain components were observed, an intrinsic strain due to the coating and an additional reactive strain that could be controlled by applying an external magnetic field to the magnetostrictive coating. Depending on the field direction, the total strain could be increased or reduced.

A powerful method for visualizing the shape and strain of nanostructures in three dimensions is coherent XRD imaging (CXDI).[26,27] With CXDI it is possible to visualize single grains, defects, and strain with high precision inside functional materials[28,29] by reconstructing the complex amplitude and phase in small nanometer to micrometer sized single crystal objects.[30–32] Due to its high crystallinity and simplicity of production, ZnO nanocrystals and rods have been a common subject.[31,33,34] CXDI was further employed to visualize the strain field inside other nanoparticles including lead,[35] polycrystalline particles in thin gold films,[28] and batteries.[29,36]

In this study, complementary techniques of reciprocal and real space analyses by means of Bragg CXDI and geometric phase analysis (GPA) performed on transmission electron microscopy (TEM) micrographs were used to visualize the 3D and the estimated relative local strain distribution in piezotronic ZnO/Au microstructures in order to understand how it affects the Schottky barrier and related electrical properties.

CXDI provides a spatial resolution of 5–50 nm and a very high strain resolution of 10^{-5}. Complimentary, modern transmission electron microscopes offer a high spatial resolution better than 100 pm but its analytical spatial resolution to lattice strains is usually limited by the radius of a virtual aperture in GPA to

1–2 nm or the electron probe diameter, for example, 2–6 nm in diffraction-based strain measurement techniques. Compared to CXDI, these techniques including GPA have a relatively poor strain resolution on the order of 2×10^{-3} in strain maps.[37] By the combination of Synchrotron- and TEM-based techniques, the inherent strain distribution can be visualized over a wide range of length scales. ZnO is ideal for such studies, because of its high crystallinity. Further information on the techniques and the sample preparation are given in the Experimental Section.

2. Reconstructed Strain Distribution from CXDI

For the CXDI experiment one of the $\{10\bar{1}0\}$ ZnO Bragg reflections of a gold coated ZnO rod was investigated. The rod was illuminated with a coherent X-ray beam using the geometry shown in **Figure 1**a. The recorded diffraction pattern around the $\{10\bar{1}0\}$ Bragg reflection in the q_x/q_z plane is shown in Figure 1b, averaged over a 0.09 Å^{-1} wide range in the q_y direction. The Bragg reflection has a full width at half maximum (FWHM) in q_x of $7.0 \times 10^{-4} \pm 0.1 \times 10^{-4}$ Å^{-1}, and a mean crystalline domain size of 927 ± 25 nm is determined. Furthermore, hexagonal symmetry and fringes from coherent scattering are clearly visible. From the fringe spacing a mean rod diameter of 940 ± 19 nm was calculated. This is in the same range as the calculated crystallite size, indicating an excellent crystal quality. From the information included in the coherent diffraction patterns of the ZnO rod, the complex amplitude of the rod's electron density was reconstructed by performing iterative phase retrieval.[38,39] Data were collected at a number of positions along the rod in the y direction corresponding to the c–axis as shown in Figure 1a and successfully reconstructed.

These positions display a very similar behavior. Here, we focus on the data for one position to avoid repetition, as it is representative for all measured positions. The reconstructed electron density amplitude is displayed in Figure 1c. Showing the corresponding reconstructed shape for three different isosurfaces with values 0.37 (1/e), 0.5, and 0.6.[41] Each isosurface connects data points of the same value inside a volume. For the further discussion only the front section between y 0 and 0.6 µm with isosurface 1/e will be considered.

In addition, CXDI measurements of the $\{10\bar{1}0\}$ Bragg reflection provide the strain component $\varepsilon_{10\text{-}10}$ along the corresponding scattering vector (indicated in Figure 1c by a black arrow). This strain component describes lattice deformation in the (0001) plane of the wurtzite-type structure (Figure 1d). The strain distribution within the rod is calculated as the gradient of the displacement field, which is the reconstructed phase divided by the scattering vector (detailed description is given in Supporting Information).[42] This reconstructed phase contains information on the relative displacements of the atoms within the crystal, that is, variations in strain. The Bragg reflection with maximum intensity on the detector was found at $q_{10\text{-}10} = 2.2319 \pm 0.0001$ Å^{-1}. A theoretical value for Zinc oxide is $q_{10\text{-}10} = 2.2324$ Å^{-1} corresponding to a lattice parameter of 2.8146 Å.[40] Comparing these values indicates a compressive global strain of 2.2×10^{-4} in the rod, relative to the theoretical value. To visualize the local strain, the reconstructed strain distribution in the sample is considered. A mean strain for the reconstructed volume is calculated by averaging the individual strain from each voxel in all three

a)

Detector

ZnO c-axis

Au coating

ZnO (10-10)

k_{out}

q

beam path

k_{in}

y

z

x

b)

Δq_x (10^{-3} Å^{-1})

Δq_z (10^{-3} Å^{-1})

log$_{10}$(Int (cts))

$\cong$ 958 nm

$\cong$ 914 nm

$\cong$ 946 nm

c)

z (µm)

y (µm)

x (µm)

Isosurface Values: 1/e 0.5 0.6

d)

Zn

O

$\varepsilon_{10\text{-}10}$

b

c

a
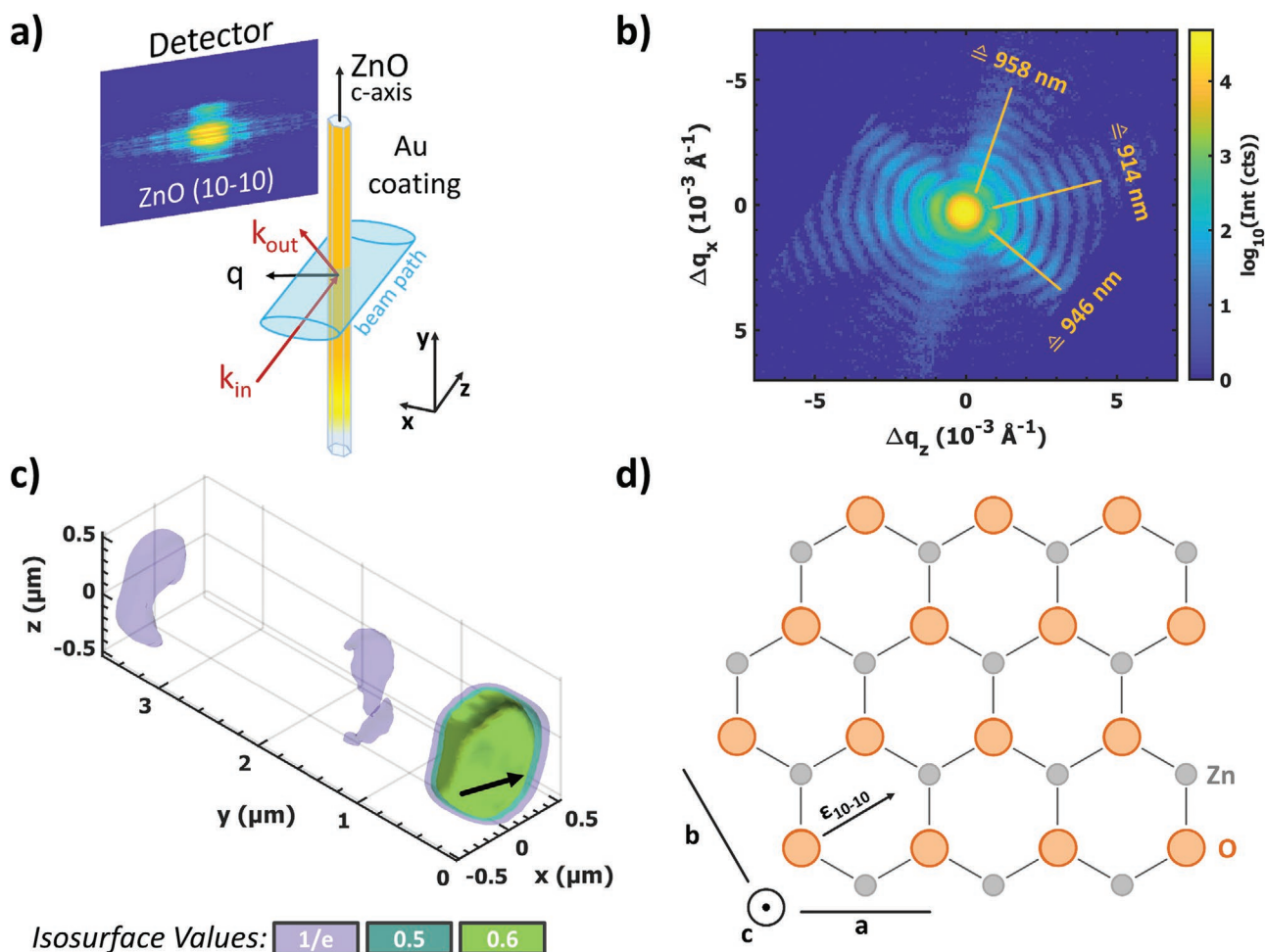
Figure 1. a) Sketch of the CXDI experiment for strain investigations of a gold coated ZnO rod. The scattering vector q of the $\{10\bar{1}0\}$ ZnO Bragg reflection, the c–axis of the ZnO, and the path of the incident beam are indicated and a coordinate system for the further analysis is introduced. The detector image is uncorrected but is approximately aligned in the q_y and q_x directions. b) Diffraction pattern shown on log scale in the q_x/q_z plane. The rod diameter calculated from the fringe spacing is indicated for three directions within the ZnO (0001) plane. c) Displaying the reconstructed shape of the rod with multiple isosurfaces of 0.37 (1/e), 0.5, and 0.6. The direction of the scattering vector q is indicated by the black arrow. d) ZnO structure in the (0001) plane[40] and the measured strain component $\varepsilon_{10\bar{1}0}$.

dimensions and found to be 5.8×10^{-5}. This is subtracted from the reconstructed strain at each point to give the relative strain distribution. The strain present in the sample is a combination of the average, global strain and the relative, reconstructed strain. For refraction corrected strain the phase shift due to the refractive index and the varying path lengths through the rod is considered[43,44] (procedure given in the SI). Furthermore, to align the scattering vector (black arrow) with the x–axis in Figure 1c, the reconstruction is rotated counterclockwise by 14.17 ° (Bragg angle). X– and Z–axis are the respective rotated positions. The 3D distribution of the reconstructed, refraction corrected, relative strain in a rod section of 0.4 µm × 1 µm × 1 µm is shown in **Figure 2**a. For better accessibility of the strain distribution inside the rod, the reconstructed volume was cut in half along the Y–axis. In agreement with literature, the interface exhibits a remarkable large strain compared to the bulk of the sample.[25] A strong compressive strain -2.2×10^{-4} is visible close to the left ZnO/Au interface, subsequently an increase of the strain is observed inside the rod. Toward the right interface a strong tensile strain 1.3×10^{-4} is observed.

From this strain distribution the average of the strain in Z direction is calculated as a function of X and shown in Figure 2b. The average strain (blue crosses) has a linear behavior near the sample center at $X \approx 0$ to 0.2 µm. Closer to the edges the strain changes drastically. Toward the right side (beginning at $X \approx 0.25$ µm) the strain increases over a range of 150 nm, before it settles and decreases closer toward the interface. On the left ($X \approx -0.1$ to -0.4 µm), the strain decreases slightly and settles over roughly 300 nm, then within the last ≈100 nm toward the interface the strain decreases further.

2.1. Strain Modeling

To quantify the strain a model was developed, consisting of a minimal constant offset, a linear component due to rod bending. Further, two exponential functions at the edges account for interface strain as previously applied[25] and two Gaussian functions are assigned to bulk strain further inside
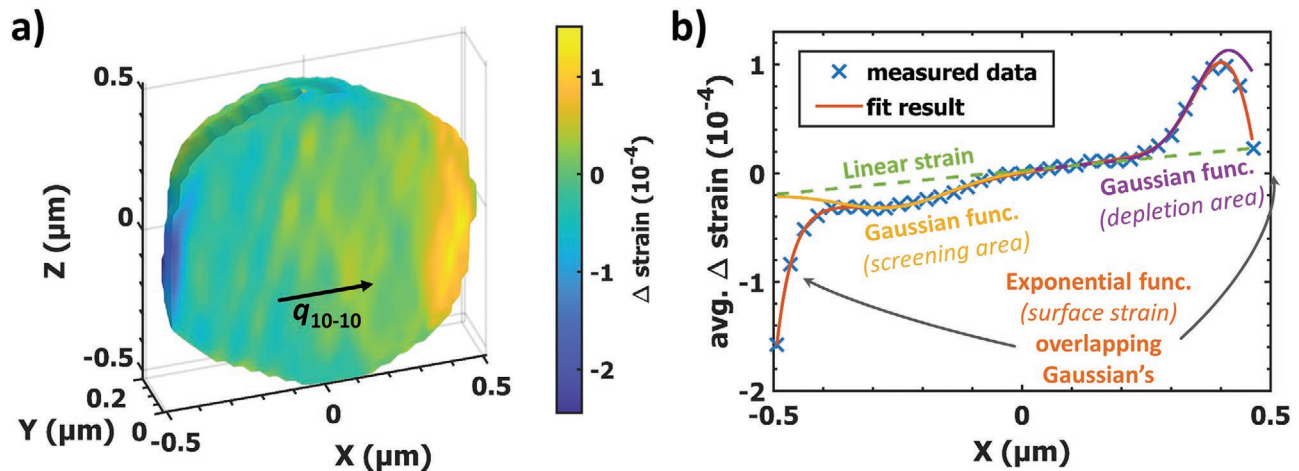
Figure 2. a) Reconstructed shape and refraction corrected strain of the ZnO rod (Isosurface 1/e) from CXDI. To illustrate the strain distribution in the X/Z-plane the reconstructed volume was cut in half in the Y-direction, with the front surface corresponding to a cross section through the center. The black arrow indicates the direction of the scattering vector $q_{10\text{-}10}$. b) Average strain along Z (blue crosses) as a function of X, from (a), shown with the fit result of the model function (solid red line), the two Gaussian components of the model (purple and yellow solid line) and the fitted linear component (green dashed line).

the crystal to consider potential screening and depletion of electrons as motivated by previous simulations,[22,23] where rod bending of a ZnO wire was shown to cause screening and depletion effects at opposing rod edges. The simulated electrical potential is linked to an electric field and causes a strain change due to the piezoelectric properties of ZnO. This model was fitted to the average strain data in Figure 2c.

$$
\begin{aligned}
\varepsilon_{avg}(X) = {} & \varepsilon_{B,CDI,l} \exp\left(\frac{-\left(X - \mu_{B,CDI,l}\right)^2}{2\,\sigma_{B,CDI,l}^2} \right) \\
& + \varepsilon_{B,CDI,r} \exp\left(\frac{-\left(X - \mu_{B,CDI,r}\right)^2}{2\,\sigma_{B,CDI,r}^2} \right) \\
& + \varepsilon_{I,CDI,l} \exp\left(\frac{-\left(X - x_1\right)}{\sigma_{I,CDI,l}} \right) \\
& + \varepsilon_{I,CDI,r} \exp\left(\frac{X - x_n}{\sigma_{I,CDI,r}} \right) + \frac{\varepsilon_{bend}}{x_n - x_1} X + \varepsilon_{const}
\end{aligned}
\tag{1}
$$

X is the position across the sample, with its first value x_1 and last value x_n inside the reconstructed volume. $\varepsilon_{B,CDI}$, $\sigma_{B,CDI}$, and $\mu_{B,CDI}$ are the fitted bulk strain, sigma, and position of the Gaussian functions, respectively. The exponential functions are fixed to the opposing edges of the rod and have values for the interface strain $\varepsilon_{I,CDI}$ and sigma $\sigma_{I,CDI}$. The subscript l and r

in the parameters of the exponential and Gaussian functions denote the position left and right relative to the rod center in Figure 2a. Furthermore, there is a linear strain ε_{bend} and a constant offset ε_{const}. The fitted $\sigma_{I,CDI}$ and $\sigma_{B,CDI}$ values can be interpreted as a measure for the spatial size of the effect, that is, the penetration depth of the surface strain and the spatial size of the bulk strain. The red solid line in Figure 2b shows the fit result of the whole model function, for a more specific look the two Gaussian functions (purple and yellow lines) as along with the linear component (green dashed line) are shown. The exponential functions at the edges are implicitly included as the difference between the overall fit result and the Gaussian functions. See **Table 1** for all values extracted from the fit model and Supporting Information for further details on the fitting procedure. The linear strain from the model indicates a tensile strain along the ZnO c–axis on the left and a compressive strain at the right edge, possibly due to the rod being bent toward the right side (radius = 6.8 mm) and may be the result of an intrinsic bending from the growth or due to the coating process. The linear behavior is overlapped by two Gaussian functions modeling the bulk strain, which show a differing but consistent behavior. The Gaussian strain component on the right is of greater magnitude, smaller width, and opposite sign compared to the one on the left. This non-symmetric distributions may be related to a potential screening and depletion of electrons in a bent rod as previously simulated.[22,23] As pointed out in

Table 1. Fit results of the model (Equation (1) for the strain ε, spatial position μ and size σ for bulk $(_{B,CDI})$ and interface $(_{I,CDI})$ strain components from CXDI reconstruction. The E field was calculated from the fitted $\varepsilon_{B,CDI}$ values. For comparison, the strain $\varepsilon_{I,TEM}$ distinguished by TEM and the measured surface strain ε_{ref} from a nano XRD experiment on FeCoSiB coated ZnO rods were included. Furthermore, strain from rod bending ε_{bend} and constant offset ε_{const} are shown.

pos.	$\sigma_{B,CDI}$ [nm]	$\mu_{B,CDI}$ [nm]	$\varepsilon_{B,CDI}$ [10^{-4}]	E [10^6 V m^{-1}]	$\sigma_{I,CDI}$ [nm]	$\varepsilon_{I,CDI}$ [10^{-4}]	$\varepsilon_{ref}{}^{a)}$ [10^{-4}]	$\varepsilon_{I,TEM}$ [10^{-3}]	ε_{bend} [10^{-4}]	ε_{const} [10^{-4}]
left	117.6 ± 6.4	233.9 ± 7.7	-0.22 ± 0.02	4.37 ± 0.22	34.9 ± 1.3	-1.36 ± 0.03	-4.0 ± 0.5	-17.5 ± 2.5	0.44 ± 0.02	0.019 ± 0.01
right	69.2 ± 1.4	45.8 ± 1.6	1.03 ± 0.02	-20.27 ± 0.28	43.0 ± 2.3	-0.83 ± 0.03				

a)From ref. [25].
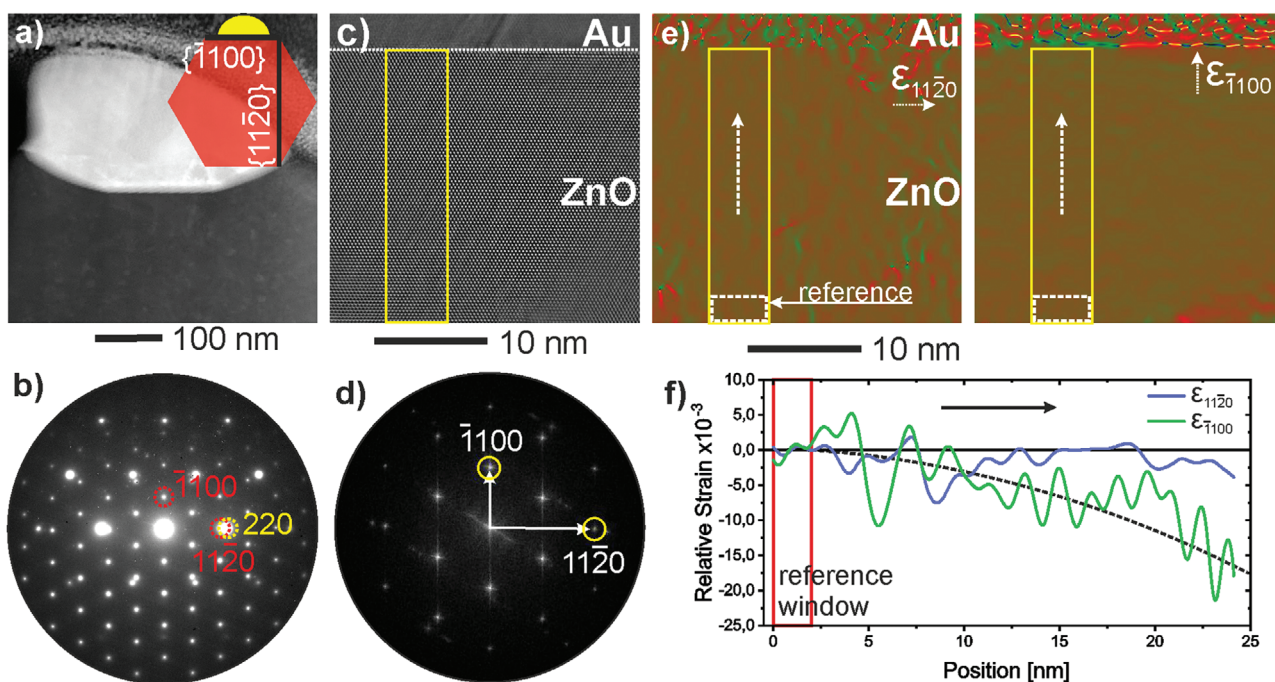
Figure 3. a) HAADF STEM image showing the cross-section of a ZnO/Au nanostructure simplified in the accompanying sketch. b) SAED pattern showing reflections of [0001] ZnO and [111] Au with ZnO($11\bar{2}0$)/Au(220) in-plane orientation relationship. c) HRTEM micrograph showing the ZnO/Au interface (dashed line) d) FFT of the HRTEM micrograph in (c) showing virtual apertures placed on in-plane and out-of-plane reflections of the ZnO component used for GPA. e) Strain distribution maps of the in-plane ($\varepsilon_{11\bar{2}0}$) and out-of-plane ($\varepsilon_{\bar{1}100}$) components of the symmetric strain tensor. The yellow boxes indicate the region for taking integrated strain profiles in relation to the selected reference lattice (white boxes). f) Estimated relative strain profiles showing increasing compressive strain in the out-of-plane component ($\varepsilon_{\bar{1}100}$) approaching the ZnO/Au interface. The dashed line serves as guide to the eye.

these publications, bending of a ZnO wire leads to a change in the potential. Considering the local potential distribution, the negative potential on one edge of the wire causes a depletion of electrons, while the positive potential on the opposite side is screened at least partially by free electrons resulting in a non-symmetric potential distribution as present in n-type semiconductor. The related electric field leads to a measurable bulk strain in the piezoelectric rod. This bulk strain is overlapped by a symmetric strain toward the interface. This strain may be the result of the Schottky barrier formation at the ZnO/Au interface due to the inverse piezoelectric effect,[45] further details on the speculative mechanism are given in Section 4. For comparison, the typical donor concentration in n-type ZnO is ≈10^{16-18} cm^{-3}.[46,47] Together with the built-in potential $\Phi_I \approx 0.5$ V[13,46] a Schottky barrier depletion width $W_d \approx 21.7 - 217.4$ nm is estimated.[13,62,63] This is in agreement with the mean width $\sigma_{I,CDI} = 39.0 \pm 6.4$ nm from Table 1 which corresponds to a calculated donor concentration of 3.1×10^{17} cm^{-3}, details on the calculation are given in Supporting Information.

3. High-Resolution TEM Strain Analysis of ZnO/Au Interface

The (sub-)microscale CXDI strain analysis is complemented by a local strain analysis from a ZnO/Au interface with nanometer resolution using aberration-corrected high-resolution TEM (HRTEM) in combination with GPA on a comparable model

system. Knowing the local strain distribution at the metal-semiconductor interface is essential for tuning the interfacial carrier transport properties across the Schottky contact as local strain can lower the barrier effectively.[48] The high spatial resolution of TEM enables to study interfacial layers or defects at or close to the interfaces, or electronically speaking the space-charge-region, as these defects provide additional electronic states in the bandgap and act as unwanted disturbance of the strain distribution.[49]

This model system consists of Au nanocrystals grown onto the {$10\bar{1}0$} facets of a ZnO microstructure as depicted in the high-angle annular darkfield image recorded in scanning TEM mode of **Figure 3**a and the supporting sketch. The cross-section specimens were prepared such that the ZnO c–axis was aligned to the viewing direction. For some of the analyzed Au crystals, this alignment allowed a direct view onto the ZnO/Au interface without superposition artifacts. These experimental conditions allowed to observe potential systematic orientation relationships and enabled the analysis of local lattice strains. Note that a certain specimen thickness was preserved to minimize potential strain relaxation effects in a thin foil.[50] Selected area electron diffraction (SAED) experiments and fast Fourier transformation (FFT) of HRTEM micrographs display the [0001] zone axis pattern for the ZnO crystal and indicate certain in-plane correlations between the components, which can be described as ZnO($11\bar{2}0$)/Au(111) in some regions and ZnO($11\bar{2}0$)/Au(220) in other ones, based on the SAED pattern in Figure 3b.

ADVANCED
SCIENCE NEWS
www.advancedsciencenews.com

ADVANCED
ELECTRONIC
MATERIALS
www.advelectronicmat.de
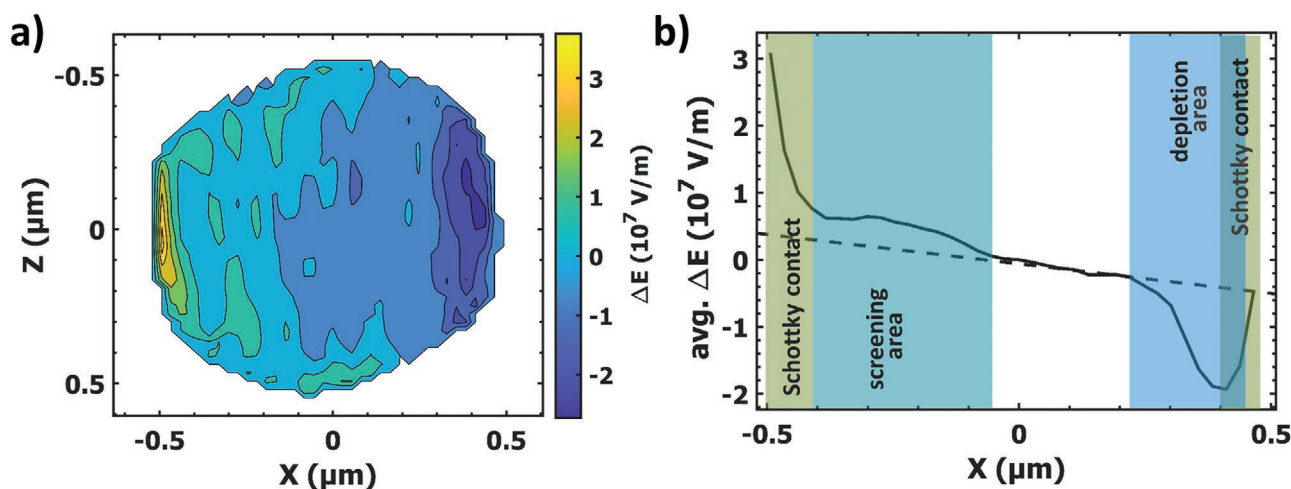
Figure 4. a) Contour plot of the E field distribution in the middle of the reconstructed volume, calculated from the strain distribution in Figure 2a. b) Average E-field calculated along the Z direction in (a), a linear increase is shown as a dashed line. Furthermore, the Schottky contact regions, screening, and depleted areas are marked.

The HRTEM micrograph (Figure 3c) does not display a sharp interface but shows a slight misorientation between the incoherent lattices of ZnO and Au. The HRTEM micrograph and corresponding FFT display the hexagonal motif viewing on the [0001] ZnO zone axis. Lattice deformations of this hexagonal motif in real space will result in broader intensities in reciprocal space and can be mapped out with respect to a presumably undistorted reference lattice within the micrograph (defect free area far away from the interface) by the GPA method.[51] The highlighted in-plane and out-of-plane reflections in Figure 3d were selected by virtual apertures limiting the spatial resolution of the strain distribution to 1.5 nm.

The relative local strain distribution in the ZnO lattice is presented in Figure 3e showing the in-plane ($\varepsilon_{11\bar{2}0}$) and out-of-plane ($\varepsilon_{\bar{1}100}$) components of the symmetric strain tensor within an experimental resolution of $\approx 5 \times 10^{-3}$, which is estimated from the oscillation amplitudes being an artifact of defining the spatial resolution by placing the virtual apertures around the reflections in the FFT. Please note that the non-uniform strain distribution in the Au component can be considered as artifact of the method as well, since GPA only maps the deformation vectors in coherent lattices defined by the virtual apertures and the reference lattice. The larger changes in strain contrast resolved in the right part of the $\varepsilon_{11\bar{2}0}$ map within the ZnO component are possibly connected to lattice imperfections exhibiting larger lattice deformation strains.

To concentrate on the effect size of an interfacial strain on a defect-free lattice, the magnitude of relative strain inside ZnO is measured by integrating across regions (yellow frames) exhibiting a homogenous contrast, hence excluding the influence of larger strain distributions around lattice defects.

The examined profiles (Figure 3f) exhibit an increasing relative compressive strain toward the interface for the out-of-plane component $\varepsilon_{\bar{1}100}$ reaching a value of $-(17.5 \pm 2.5) \times 10^{-3}$ and is distributed rather monotonously around zero strain for the in-plane component $\varepsilon_{11\bar{2}0}$.

In conclusion, despite interfacial layers, which are often chemically or structurally modified prior to Au-film deposition, an increasing compressive ZnO lattice structure is observed close to the ZnO/Au interface within the analytic capabilities of HRTEM and GPA.

This interfacial strain which was measured across 25 nm and with a lateral resolution of 1.5 nm increases toward the interface up to a value of $\varepsilon_{\bar{1}100, TEM} = -(17.5 \pm 2.5) \times 10^{-3}$ and is compared to the CXDI results of an interface strain reaching up to $\varepsilon_{I,CDI} = -1.4 \times 10^{-4}$ within a spatial resolution of 27.4 nm. The strain difference of two orders of magnitude is possibly due to the individual strengths in spatial and reciprocal resolution of both techniques. TEM detects a higher strain in a very localized spatial region. In contrast CXDI shows a lower strain but distributed over a larger spatial region. Extrapolating the CXDI strain toward the interface provides qualitative agreement. The discrepancy between the two results cannot be attributed completely to the differences in resolution of the two techniques. The different methodology of establishing ZnO/Au contacts for CXDI and TEM measurements might also have an impact on absolute strain values. For the CXDI experiment, an Au layer was deposited by thermal evaporation to achieve a uniform coating, while the Au contact for TEM experiments has been prepared by sputtering a thin Au film and subsequent annealing to establish small Au crystalline droplets on the ZnO surface. The higher crystallinity of these droplets and better contact quality at the Au/ZnO interface might impose an increased magnitude of strain on the ZnO crystal. Concluding that, while both methods show a similar trend in this case, we are at the limit of their accuracy. Thus, a combination of TEM and CXDI highlights the fact that a strong, highly localized compressive strain is present at the ZnO/Au interface.

4. Electric Field E_z Calculated from Strain

Of major interest is the impact of the interface and bulk strain on the electrical properties. Therefore, we calculate the E field inside the crystal from the reconstructed strain (Figure 2a) by employing the relation between the strain and the E field;

ADVANCED
SCIENCE NEWS
www.advancedsciencenews.com

ADVANCED
ELECTRONIC
MATERIALS
www.advelectronicmat.de

$\varepsilon_{ij} = d_{ijk} E_k$.[52] A more specific explanation is given in Supporting Information. For the measured strain ε_x, the corresponding E field E_z points along the c–axis of the ZnO rod and they are coupled by the piezoelectric strain coefficient $d_{31} = -5.1$ pC/N.[53] Since d_{31} has a negative value the calculated E field is inverted with respect to the strain.

The relative E field is shown in **Figure** 4a for a cut through the middle of the reconstructed volume. Therein, a strong negative E field of -2.7×10^7 V m^{-1} is located near the right edge, toward the middle of the rod it is rising to a mean value of around 0 V m^{-1} and then rises further to positive field strength of up to 4.2×10^7 V m^{-1} near the left edge. A positive field of $\approx 1 \times 10^7$ V m^{-1} is distributed around the center in a semi-circle manner toward the left. For Figure 4b the average relative E field value is calculated and shows a similar but inverted behavior to the average strain in Figure 2b. In the left region from X –0.1 to –0.3 µm the relative E field increases slowly to a maximum of 0.4×10^7 V m^{-1}, on the right in contrast we see a rapid decrease from X 0.25 to 0.4 µm reaching -2.0×10^7 V m^{-1}. All the quantitative values were fitted with the strain model and are presented in Table 1 There are four distinct areas of the E field and these may result from depletion and screening processes inside the rod, and further the coating and Schottky contact depletion region near the surface.

The compressive strain close to the interface, observed with both, TEM and XRD techniques, is likely the result from Au coating the ZnO surface. The Au coating may change the ZnO structure in at least two possible ways. Although the coating process is likely to induce a strain as proposed previously,[25] it was shown that for micro structures the thickness of a microrod coating does not exhibit a strong effect on the intrinsic strain of the piezoelectric component and that rather the rod diameter has the main effect on strain. This has also been observed for thinZnO films.[54] Additional strain may arise from the Schottky contact at the ZnO/Au interface. The proposed mechanism for the strain change at the interface is that the Schottky contact induces a potential and causes an electron depletion in the Schottky depletion region due to barrier formation. The related change of the electric field in vicinity of the Au interface leads to an impact on the crystalline structure, due to strain arising from the inverse piezoelectric effect.[45] A mechanical deformation of a piezoelectric component induces an electrical polarization, which can be measured as a piezoelectric voltage. In case of the inverse piezoelectric effect, polarization of charge centers in the material gives rise to a mechanical strain. The electron depletion from the ZnO at the Schottky barrier gives rise to localized positive charge and thus polarized charge centers causing a local mechanical deformation. The measured width of the interface strain $\sigma_{I,CDI}$ agrees with the calculated Schottky depletion width, as shown prior, and supports this mechanism as a source of interface strain. This explanation is a hypothesis, further experiments are required to achieve a better insight and understanding of the underlying effect. A possible path could be a measurement of the full strain tensor, by, for example, CXDI, and additional impedance spectroscopy to distinguish the Schottky barrier depletion width.

The macroscopic bending of the rod must be considered, as well. The non-symmetric strain distribution observed in Figure 2 can be explained by considering the E field distribution as shown in Figure 4, describing screening and depletion processes inside a bent, piezotronic rod.[23] However, to verify this unambiguously one would need to distinguish which of the two regions is depleted and which is screened. This is extremely challenging. Here, we consider that the E field is defined as force per charge, for example, $E_z = F_z/q$, a weaker E field leads to a smaller force accelerating the electrons. Thus, the electron density is likely to be higher in the compressed region (left hand side Figure 2b) and screens a positive potential more effectively. In comparison, the relaxed region on the right side of the rod results in a lower electron density due to the stronger force and thus electron depletion occurs. A similar effect has been proposed by Wang and Song to explain conduction behavior in a bent, piezotronic ZnO nanorod.[21] They also predict that introducing doping electrons to this system results in depletion of electrons and screening of the positive potential.[23] This is consistent with our results, as n-type ZnO was used in this experiment. CXDI provides a direct visualization and quantification of these effects.

5. Conclusion

TEM and CXDI techniques were combined to investigate and visualize the strain distribution of ZnO microstructures attached to Au. A strain was found at the ZnO/Au interface, likely to be a combination of strain induced by coating and strain due to the inverse piezoelectric effect at the Schottky contact. Furthermore, a non-symmetrical strain distribution inside the ZnO rod is attributed to depletion of electrons and screening of the positive potential due to rod bending. The high strain concentration at the coated microrod interface indicates a high potential for applications using piezotronic devices. The study of strain localization may advance the development of small electronic devices in the future, as already demonstrated for transistors based on the piezotronic effect.[55] Furthermore, highly sensitive and small sensors, based on piezotronics, may enable the design of portable sensors arrays, dedicated to measurement of biomagnetism from the human physiology, for example, from the brain or heart, and this without the need for heavy and expensive equipment.

6. Experimental Section

Bragg CXDI: The experiment was conducted at the beamline ID-34c of the Advanced Photon Source with a photon energy of 9 keV. The beam size was focused with a Kirkpatrick–Baez mirror and a slit was used to achieve the final beam size of 2000×450 nm^2 (h × v). The data were acquired by a timepix detector with 55 µm square sized pixels and at a detector sample distance of 2.8 m. A data series of the reciprocal space around the {10$\bar{1}$0} Bragg peak was collected by rotating the sample around the ZnO's c–axis in a range of 0.24 ° with a 0.002 ° step size. For the reconstruction of the complex electron density a combination of error reduction (ER) and Hybrid-Input-Output (HIO) algorithms were used.[38,39,56,57] Each 20 ER algorithm runs were followed by 180 HIO algorithm repetitions, with a total of 1020 runs. The shape was defined by a shrink wrap algorithm.[58] A low to high resolution reconstruction was performed by changing the sigma of the Gaussian mask in the shrink wrap routine from 3 to 1 and a partial coherence correction was employed.[59,60] For every measured scan 200 reconstructions with

random starts were done to achieve a statistically reasonable result. An error metric calculated for every reconstruction was used to evaluate and pick the best results (see Supporting Information). The chosen reconstructions were correlated and a final reconstruction was calculated. The voxel size of the reconstructions was $27.4 \times 27.4 \times 27.4$ nm^3.

TEM: GPA was directly applied to the FFT of HRTEM image, which was modulated by the contrast transfer function (effect of spherical aberration and defocus mainly) to calculate lattice displacements with respect to a reference lattice with nanometer resolution and minimum 2×10^{-3} strain precision. The following microscopes were used during this study: A Tecnai F30 G² (300 kV, field emission gun (FEG)) and a Titan 80–300 operated at 300 kV equipped with an image corrector to correct spherical aberrations for HRTEM imaging. GPA was performed using a plug-in tool (FRWRtools plug-in, Christoph T. Koch, HU Berlin, Institute of Physics) for DigitalMicrograph.

Sample Preparation: To produce the ZnO microstructures the flame transport synthesis was used.[61] With this technique, it was possible to produce tailor made ZnO rods with diameters ranging from below 1 μm to a few hundred μm and lengths up to mm. The diameter of the measured ZnO rod was 1.0 ± 0.2 μm. One end of the rod was fixed to a glass capillary by adhesive, the other end was free standing. The sample was coated with 50 nm gold in a thermal evaporation physical vapor deposition process from two opposing directions. The layer thickness was distinguished by measuring the deposition rate with a quartz crystal microbalance. For the TEM a model system exhibiting larger Au nanocrystals (diameter of 200 – 500 nm) on the ZnO surface was prepared by sputter deposition of a thin gold layer and subsequent annealing to 600 °C. A thin cross-section specimen containing these ZnO/Au interfaces was prepared by focused ion beam technique cutting the ZnO microrod perpendicular to the (0001) plane.

Supporting Information

Supporting Information is available from the Wiley Online Library or from the author.

Conflict of Interest

The authors declare no conflict of interest.

Data Availability Statement

The data that support the findings of this study are available from the corresponding author upon reasonable request.

[1] W. Wu, X. Wen, Z. L. Wang, *Science* **2013**, *340*, 952.
[2] Y. Chen, G. Gao, J. Zhao, H. Zhang, J. Yu, X. Yang, Q. Zhang, W. Zhang, S. Xu, J. Sun, Y. Meng, Q. Sun, *Adv. Funct. Mater.* **2019**, *29*, 1900959.
[3] Y. S. Zhou, K. Wang, W. Han, S. C. Rai, Y. Zhang, Y. Ding, C. Pan, F. Zhang, W. Zhou, Z. L. Wang, *ACS Nano* **2012**, *6*, 6478.
[4] L. Zhou, T. Yang, L. Zhu, W. Li, S. Wang, X. Hou, X. Mao, Z. L. Wang, *Nano Energy* **2021**, *83*, 105826.
[5] Y. Zhou, D. Maurya, Y. Yan, G. Srinivasan, E. Quandt, S. Priya, *Energy Harvesting Syst.* **2015**, *3*, 1.
[6] E. Lage, C. Kirchhof, V. Hrkac, L. Kienle, R. Jahns, R. Knöchel, E. Quandt, D. Meyners, *Nat. Mater.* **2012**, *11*, 523.
[7] J. Ma, J. Hu, Z. Li, C.-W. N. Nan, *Adv. Mater.* **2011**, *23*, 1062.
[8] P. Hayes, S. Salzer, J. Reermann, E. Yarar, V. Röbisch, A. Piorra, D. Meyners, M. Höft, R. Knöchel, G. Schmidt, E. Quandt, *Appl. Phys. Lett.* **2016**, *108*, 182902.
[9] W. Liu, A. Zhang, Y. Zhang, Z. L. Wang, *Nano Energy* **2015**, *14*, 355.
[10] L. Wang, Z. L. Wang, *Nano Today* **2021**, *37*, 101108.
[11] J. Gröttrup, S. Kaps, J. Carstensen, D. Smazna, Y. K. Mishra, A. Piorra, C. Kirchhof, E. Quandt, R. Adelung, *Phys. Status Solidi A* **2016**, *213*, 2208.
[12] M. Mintken, M. Schweichel, S. Schröder, S. Kaps, J. Carstensen, Y. K. Mishra, T. Strunskus, F. Faupel, R. Adelung, *Nano Energy* **2019**, *56*, 420.
[13] S. M. Sze, K. K. Ng, *Physics of Semiconductor Devices*, 3rd ed., Wiley, New York **2006**.
[14] R. Martin, *Phys. Rev. B* **1972**, *5*, 1607.
[15] S. G. Louie, J. R. Chelikowsky, M. L. Cohen, *Phys. Rev. B* **1977**, *15*, 2154.
[16] P. Keil, T. Frömling, A. Klein, J. Rödel, N. Novak, *J. Appl. Phys.* **2017**, *121*, 155701.
[17] P. Jordt, N. Wolff, S. B. Hrkac, S. Shree, D. Wang, R. J. Harder, C. Kübel, R. Adelung, O. G. Shpyrko, O. M. Magnussen, B. M. Murphy, *Adv. Eng. Mater.* **2021**, 2100201. https://doi.org/10.1002/adem.202100201.
[18] J. Zhou, Y. Gu, P. Fei, W. Mai, Y. Gao, R. Yang, G. Bao, Z. L. Wang, *Nano Lett.* **2008**, *8*, 3035.
[19] W. Wu, Y. Wei, Z. L. Wang, *Adv. Mater.* **2010**, *22*, 4711.
[20] Z. Gao, J. Zhou, Y. Gu, P. Fei, Y. Hao, G. Bao, Z. L. Wang, *J. Appl. Phys.* **2009**, *105*, 113707.
[21] Z. L. Wang, J. Song, *Science* **2006**, *312*, 242.
[22] Y. Gao, Z. L. Wang, *Nano Lett.* **2007**, *7*, 2499.
[23] Y. Gao, Z. L. Wang, *Nano Lett.* **2009**, *9*, 1103.
[24] S. B. Hrkac, M. Abes, C. T. Koops, C. Krywka, M. Müller, S. Kaps, R. Adelung, J. McCord, E. Lage, E. Quandt, O. M. Magnussen, B. M. Murphy, M. Müller, S. Kaps, R. Adelung, J. McCord, E. Lage, E. Quandt, O. M. Magnussen, B. M. Murphy, *Appl. Phys. Lett.* **2013**, *103*, 123111.
[25] S. B. Hrkac, C. T. Koops, M. Abes, C. Krywka, M. Müller, M. Burghammer, M. Sztucki, T. Dane, S. Kaps, Y. K. Mishra, R. Adelung, J. Schmalz, M. Gerken, E. Lage, C. Kirchhof, E. Quandt, O. M. Magnussen, B. M. Murphy, *ACS Appl. Mater. Interfaces* **2017**, *9*, 25571.
[26] I. Robinson, R. Harder, *Nat. Mater.* **2009**, *8*, 291.

ADVANCED
SCIENCE NEWS
www.advancedsciencenews.com

ADVANCED
ELECTRONIC
MATERIALS
www.advelectronicmat.de

[27] F. Hofmann, N. W. Phillips, S. Das, P. Karamched, G. M. Hughes, J. O. Douglas, W. Cha, W. Liu, *Phys. Rev. Mater.* **2020**, *4*, 013801.

[28] A. Yau, W. Cha, M. W. Kanan, G. B. Stephenson, A. Ulvestad, *Science* **2017**, *356*, 739.

[29] A. Ulvestad, A. Singer, H. M. Cho, J. N. Clark, R. Harder, J. Maser, Y. S. Meng, O. G. Shpyrko, *Nano Lett.* **2014**, *14*, 5123.

[30] S. Lazarev, D. Dzhigaev, Z. Bi, A. Nowzari, Y. Y. Kim, M. Rose, I. A. Zaluzhnyy, O. Y. Gorobtsov, A. V. Zozulya, F. Lenrick, A. Gustafsson, A. Mikkelsen, M. Sprung, L. Samuelson, I. A. Vartanyants, *Nano Lett.* **2018**, *18*, 5446.

[31] M. C. Newton, S. J. Leake, R. Harder, I. K. Robinson, *Nat. Mater.* **2010**, *9*, 17.

[32] Y. Gao, R. Harder, S. H. Southworth, J. R. Guest, X. Huang, Z. Yan, L. E. Ocola, Y. Yifat, N. Sule, P. J. Ho, M. Pelton, N. F. Scherer, L. Young, *Proc. Natl. Acad. Sci. U. S. A.* **2019**, *116*, 4018.

[33] X. Huang, R. Harder, S. Leake, J. Clark, I. Robinson, *J. Appl. Crystallogr.* **2012**, *45*, 778.

[34] G. Xiong, X. Huang, S. Leake, M. C. Newton, R. Harder, I. K. Robinson, *New J. Phys.* **2011**, *13*, 033006.

[35] M. A. Pfeifer, G. J. Williams, I. A. Vartanyants, R. Harder, I. K. Robinson, *Nature* **2006**, *442*, 63.

[36] F. Lin, F. Liu, X. Yu, L. Cheng, A. Singer, O. G. Shpyrko, H. L. Xin, N. Tamura, C. Tian, T. C. Weng, X. Q. Yang, Y. S. Meng, D. Nordlund, W. Yang, M. M. Doeff, *Chem. Rev.* **2017**, *117*, 13123.

[37] D. Cooper, T. Denneulin, N. Bernier, A. Béché, J. L. Rouvière, *Micron* **2016**, *80*, 145.

[38] J. R. Fienup, *Appl. Opt.* **1982**, *21*, 2758.

[39] J. R. Fienup, C. C. Wackerman, *J. Opt. Soc. Am. A* **1986**, *3*, 1897.

[40] K. Ellmer, A. Klein, B. Rech, *Transparent Conductive Zinc Oxide*, Springer-Verlag, Berlin, Heidelberg **2008**.

[41] J. Carnis, L. Gao, S. Labat, Y. Y. Kim, J. P. Hofmann, S. J. Leake, T. U. Schülli, E. J. M. M. Hensen, O. Thomas, M. I. Richard, L. Stéphane, Y. Y. Kim, J. P. Hofmann, J. L. Steven, U. S. Tobias, E. J. M. Hensen, O. Thomas, M.-I. Richard, *Sci. Rep.* **2019**, *9*, 17357.

[42] G. Xiong, O. Moutanabbir, M. Reiche, R. Harder, I. Robinson, *Adv. Mater.* **2014**, *26*, 7747.

[43] R. Harder, M. A. Pfeifer, G. J. Williams, I. A. Vartaniants, I. K. Robinson, *Phys. Rev. B* **2007**, *76*, 115425.

[44] V. Favre-Nicolin, F. Mastropietro, J. Eymery, D. Camacho, Y. M. Niquet, B. M. Borg, M. E. Messing, L. E. Wernersson, R. E. Algra, E. P. A. M. Bakkers, T. H. Metzger, R. Harder, I. K. Robinson, *New J. Phys.* **2010**, *12*, 035013.

[45] S. N. Levine, *J. Appl. Polym. Sci.* **1965**, *9*, 3351.

[46] J.-J. Wu, D. K.-P. Wong, *Adv. Mater.* **2007**, *19*, 2015.

[47] K. I. Hagemark, L. C. Chacka, *J. Solid State Chem.* **1975**, *15*, 261.

[48] X. Ma, Y. Dai, L. Yu, B. Huang, *Nanoscale* **2016**, *8*, 1352.

[49] S. B. Lee, J. W. Ju, Y. M. Kim, S. J. Yoo, J. G. Kim, H. N. Han, D. N. Lee, *AIP Adv.* **2015**, *5*, 077180.

[50] R. Hull, *Appl. Phys. Lett.* **1993**, *63*, 2291.

[51] M. J. Hÿtch, L. Potez, *Philos. Mag. A* **1997**, *76*, 1119.

[52] H. Morkoç, Ü. Özgür, *Zinc Oxide : Fundamentals, Materials and Device Technology*, Wiley, New York **2008**.

[53] M. Catti, Y. Noel, R. Dovesi, *J. Phys. Chem. Solids* **2003**, *64*, 2183.

[54] V. Kumar, S. K. Singh, H. Sharma, S. Kumar, M. K. Banerjee, A. Vij, *Phys. B* **2019**, *552*, 221.

[55] L. Wang, S. Liu, G. Gao, Y. Pang, X. Yin, X. Feng, L. Zhu, Y. Bai, L. Chen, T. Xiao, X. Wang, Y. Qin, Z. L. Wang, *ACS Nano* **2018**, *12*, 4903.

[56] H. H. Bauschke, P. L. Combettes, D. R. Luke, *J. Opt. Soc. Am. A* **2002**, *19*, 1334.

[57] S. Marchesini, *Rev. Sci. Instrum.* **2007**, *78*, 011301.

[58] S. Marchesini, H. He, H. N. Chapman, S. P. Hau-Riege, A. Noy, M. R. Howells, U. Weierstall, J. C. H. Spence, *Phys. Rev. B* **2003**, *68*, 140101.

[59] I. A. Vartanyants, I. K. Robinson, *J. Phys.: Condens. Matter* **2001**, *13*, 10593.

[60] J. N. Clark, X. Huang, R. Harder, I. K. Robinson, *Nat. Commun.* **2012**, *3*, 993.

[61] Y. K. Mishra, S. Kaps, A. Schuchardt, I. Paulowicz, X. Jin, D. Gedamu, S. Freitag, M. Claus, S. Wille, A. Kovalev, S. N. Gorb, R. Adelung, *Part. Part. Syst. Charact.* **2013**, *30*, 775.

[62] F. S. Mahmood, R. D. Gould, A. K. Hassan, H. M. Salih, *Thin Solid Films* **1995**, *270*, 376.

[63] R. Ondo-Ndong, H. Essone-Obame, Z. H. Moussambi, N. Koumba, *J. Theor. Appl. Phys.* **2018**, *12*, 309.